Materials & Design 241 (2024) 112913

Contents lists available at ScienceDirect

Materials & Design

journal homepage: www.elsevier.com/locate/matdes

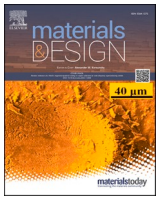

Design and macroscopic mechanical responses of auxetic metamaterials with tunable stiffness

Shangbin Wang [a], Junxian Guo [a,b,*], Andras Biczo [c], Ning Feng [d,*]

[a] College of Mechanical and Electrical Engineering, Xinjiang Agricultural University, Urumqi 830052, China
[b] Key Laboratory of Xinjiang Intelligent Agricultural Equipment, Urumqi 830052, China
[c] Department Hamm 2, Hamm-Lippstadt University of Applied Sciences, Hamm 59063, Germany
[d] School of Electrical and Mechanical Engineering, Pingdingshan University, Pingdingshan 467000, China

ARTICLE INFO

Keywords:
Auxetic
Coupling mechanical metamaterials system
Energy principle
Elastic properties

ABSTRACT

This research presents the design, manufacturing, and macroscopic characterization of flexible mechanical metamaterials with tunable elastic properties. The elastic constants were given using the energy principle and Castigliano's second theorem, and the results were validated through static simulations and tensile experiments, showing good agreement. Then the complete parametric study was conducted to demonstrate the possibility of extensively customizing the Poisson effect and stiffness. Additionally, the comparison between the developed metamaterials and star-shaped cellular structures on the mechanical properties was conducted using six groups of samples. The results demonstrated that the developed metamaterials exhibited remarkable superiority in deformability, sensitivity, and auxeticity. Furthermore, an innovative experiment is devised to characterize the mechanical responses of the developed coupling metamaterials system complemented with numerical modeling, the similar phenomenon was also observed in other metamaterials. The proposed design offered a way to induce the metamaterials system's profile occurring the wavy deformation.

1. Introduction

Generally, mechanical metamaterials are particularly defined as artificial structural materials that can achieve unprecedented properties through their unique microstructural design [1–5]. Nowadays, increasingly considerable research focuses on designing [6–8], fabricating [9,10], and characterizing mechanical metamaterials [11,12]. Further, their remarkable performance is employed in multifarious applications [13]. One of the fascinating features of metamaterials is their auxetic effect [14–16]. Unlike conventional materials that contract laterally when stretched, the auxetic metamaterials expand laterally [17]. The auxetic metamaterials find applications in various fields, including impact absorption [18,19], vibration damping [20,21], and flexible electronics [22,23]. Another exceptional property of metamaterials is negative stiffness [24–28], they resist deformation under applied forces, metamaterials can compress under tension and expand under compression [29]. This unique behavior is achieved through the arrangement of substructures that induce buckling or snap-through instabilities [30]. Negative stiffness metamaterials have potential applications in shock absorption [31], energy harvesting [32], and soft robotics [31]. Metamaterials can also offer exceptional wave manipulation properties like negative refraction [33,34], cloaking [35], wave focusing [36], and waves transition [37]. These properties enable the development of devices such as acoustic lenses [38] and vibration dampers [39–42], which have practical applications in noise control [43], waveguiding [44–46], and imaging [47].

Routinely, mechanical metamaterials are designed by tailoring the geometric feature and arrangement of their constituent elements at the microscale. The design principles involve purposefully engineering the prototype of the unit cells to obtain desired mechanical functionalities. Common design strategies include lattice structures [48], hierarchical structures [49], origami-inspired structures [50], and kirigami-based structures [51]. Lattice structures are repetitive patterns of interconnected unit cells that form the element of metamaterials. Examples of lattice structures include honeycomb structures [52,53], diamond lattices [54], and triply periodic minimal surfaces [TPMS] structures [55,56]. TPMS structures have a continuous, smooth surface and are characterized by minimal surface area. Hierarchical structures involve

* Corresponding authors at: School of Electrical and Mechnical Engineering, Pingdingshan University, Pingdingshan 467000, China (N. Feng); College of Mechanical and Electrical Engineering, Xinjiang Agricultural University, Urumqi 830052, China(J. Guo).
E-mail addresses: junxianguo@163.com (J. Guo), fengning@pdsu.edu.cn (N. Feng).

https://doi.org/10.1016/j.matdes.2024.112913
Received 8 January 2024; Received in revised form 28 March 2024; Accepted 1 April 2024
Available online 2 April 2024

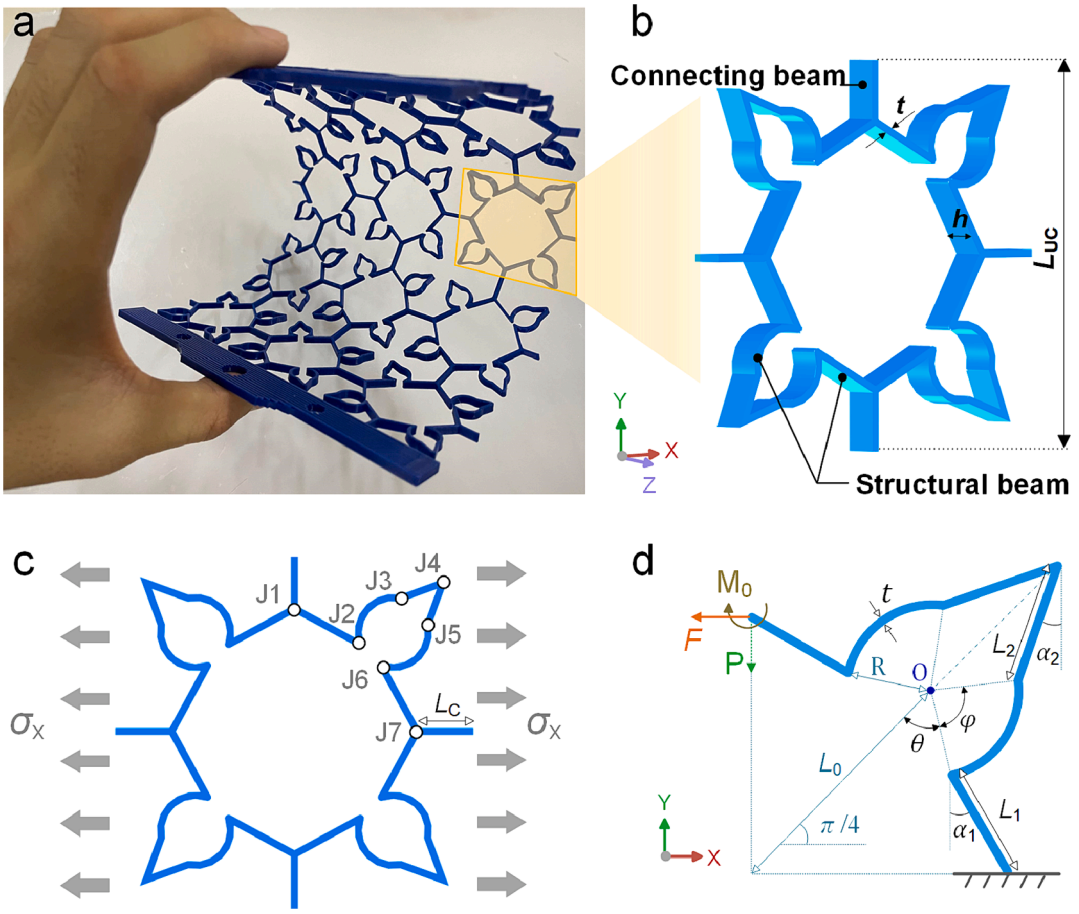

Fig. 1. (a) An sample of the developed mechanical metamaterials, showing their highly flexible nature; (b) unit cell, (c) loading scheme, (d) quatered free body diagram.

in corporating multiple length scales into the design of metamaterials. By combining different levels of structural organization, hierarchical metamaterials can achieve enhanced mechanical properties [57]. This approach allows for the optimization of material distribution and the manipulation of mechanical behavior at different scales. Studies on the star-shaped structures are continuously conducted. The tetra-petals metamaterials are optimized via a systematic isogeometric design approach [58], this research also presented the potential application for the functionally graded metamaterials. The auxetic responses of a novel series of planar periodic metamaterials named as “connected-stars” are investigated [59], the structures possess star-shaped cells of various rotational symmetries. A class of general Star-4 structures’ Poisson’s ratio was investigated theoretically, numerically, and experimentally [60], this research found that the different thickness of the structural ligaments may lead to a more remarkable auxetic effect. Origami, the art of paper-folding, has inspired the development of metamaterials with unique mechanical properties. By applying principles of origami, researchers have created foldable and deployable structures that can undergo large deformations [61] while maintaining their structural integrity. Kirigami, the art of papercutting [62], the incorporation of kirigami techniques into metamaterial design then create structures that can undergo large deformations and exhibit tunable mechanical performances. Through the strategic arrangement of cuts and folds, these kirigami-based materials can deform in specific ways, such as stretching [63], twisting [64], or bending [65]. This property makes them suitable for applications requiring shape morphing [66], such as soft robotics [67], adaptive structures [68], and biomedical devices [69]. Metamaterials can also be designed using other strategies, such as topology optimization, where the improvement is made to the material distribution within the designated design space to realize specific mechanical characteristics. Additive manufacturing technology, such as fused deposition modeling, allows for the fabrication of intricate metamaterial structures while maintaining powerful control over their geometry and properties.

Metamaterials designed with innovative approaches are also fascinating, the flexible metamaterials introducing orthogonal perforations were designed, fabricated [70], and mechanically characterized. The finding indicates different structural perforation arrangements result in a broad spectrum of Poisson’s ratios (from −0.8 to 0.4), load-bearing abilities, and even energy absorption abilities. Another study devised and analyzed two classes of bi-material missing rib-type anti-chiral metamaterials [71], the results demonstrate the design demonstrate a variety of unique characteristics, such as being lightweight, featuring a highly customizable coefficient of thermal expansion with isotropic properties, and maintaining steady Poisson’s ratios. Also fascinatingly, the higherorder moving-mesh method was employed to customize the structural geometric features as they see fit and adjust their nonlinear mechanical property for various loading conditions [72]. The results reveal that the aperiodicity offers new possibilities for creating flexible metamaterials. Moreover, a new Poisson’s ratio (PR) sign-switching stiffness-changing mechanical metamaterial is devised, showcasing potential applications in the automotive and construction industries [73]. The metamaterial shows approximately 25 % higher specific energy absorption (SEA) properties than the hexagonal lattice structure, the metamaterial’s auxeticity and load-bearing ability could be adjusted by transforming the geometric features.

In this work, a mechanical metamaterial with tunable elastic properties was devised, and its macroscopic mechanical response was

investigated theoretically, computationally, and experimentally. The elastic constants are given by employing the energy principle and Castigliano's second theorem. Then the theoretical results are sufficiently verified by static simulation and tensile experiment, which agree well. The excellent flexibility, programmability, and deformability of the proposed metamaterials are exhibited. Multidimensional mechanical properties between the developed metamaterials and the star-shaped cellular structures are compared, the former's superiority is remarkable. An innovative experiment was devised to characterize the mechanical response of the coupling metamaterials system, which successfully induced the metamaterials system's profile occurring the wavy deformation.

2. Design

In this section, after designing the prototype of the initial unit cell, we devise a flexible mechanical metamaterial with rib-type. The relative density of the proposed metamaterial is given first, and then their elastic properties are deduced by employing the energy principle on the simplified static model.

2.1. Geometric prototype and parameters

Flexible planar samples with repeating unit cells were fabricated (Fused Filament Fabrication-FFF), as displayed in Fig. 1(a). The geometric features of the developed cellular metamaterials are shown in Fig. 1(b) and (d). Fig. 1(c) shows that the devised unit prototype is composed of four-fold symmetric homogeneous structural beams and a couple of orthogonal connecting beams, all the beams are constructed with identical thickness (t) and height (h). The longitudinal and transverse dimensions of the whole unit cells (L_{UC}) are equivalent thanks to the structural symmetry. The axial loading schematic is displayed in Fig. 1(c), the joints in the quartered free-body structure are marked as J_i ($i = 1, 2, \ldots 7$) orderly.

Key geometry attributes of the metamaterials are shown in Fig. 1(d), including the central angle θ and φ (used to locate the starting and end point of the arc line, respectively), the ligament angle α_1 and α_2 (used to determine the length L_1 and L_2, respectively). The axial loading schematic of the unit cell is displayed in Fig. 1(c), the joints in the quartered free-body structure are marked as J_i ($i = 1, 2, \ldots 7$) orderly. Note that the center of the arc line "O" is fixed by the ratio $L_0/L_{UC} = 0.4$ and the intersection angle with the horizontal auxiliary line $\pi/4$, and the radius of the arc line R is fixed by the ratio $R/L_{UC} = 0.1$, respectively.

2.2. Relative density

For the cellular metamaterials, the intrinsic porosity gives them excellent lightweight performance. By substituting the areas occupied by beams and the area of the unit cell, the relative density of the mechanical metamaterials can be deduced as

$$\begin{cases} \rho_{SSP} = \dfrac{A_S}{A_W} = \dfrac{4t(2L_1 + 2L_2 + 2R\phi + L_C)}{L_{UC}^2} \\ L_C = \dfrac{L_{UC}}{2} - \left[L_0\cos\dfrac{\pi}{4} - R\sin(\dfrac{\pi}{4} - \theta) + L_1\sin\alpha_1\right] \\ L_1 = \dfrac{L_0\cos\dfrac{\pi}{4} - R\cos(\dfrac{\pi}{4} - \theta)}{\cos\alpha_1} \\ L_2 = \dfrac{R\sin(\dfrac{\pi}{2} - \theta)}{\sin(\dfrac{\pi}{4} - \alpha_2)} \end{cases} \tag{1}$$

Here, A_S and A_W represent the area of the beams and the whole unit cell, and L_C represents the length of the connecting beam, respectively.

3. Theoretical model

In this section, the developed cellular metamaterials are assumed as a continuous medium, its elastic property is solved by the macroscopic elastic constitutive equation. The equivalent elastic properties of the cellular metamaterials are calculated by employing the energy principle and Castigliano's Second Theorem. All the connecting beams and structural beams are slender enough to be regarded as Euler-Bernoulli beams.

3.1. Elastic modulus

When the ligament is broken at J1, the free-body structure is in static equilibrium under the effect of both inner force F and unknown bending moment M_0.

Following the theory of the energy principle, when a mechanical system is statically loaded the strain energy stored (V_ε) equals the work (W) performed by the external force. To simplify the theoretical model, only the contribution of bending load is considered which can be deduced as

$$W = V_\varepsilon = \sum_{i=1}^{n} \int_{l_i} \frac{M_i(x)^2}{2E_i I_{zi}} dx \tag{2}$$

Here, M_i is moment of the structural beams, E_i is the Young's modulus of the basic materials, and I_{zi} is the second moment of beam area, respectively.

In Fig. 1(c), there is no angular distortion of the cross-section at J1 which is regarded as the deformation coordination condition to formulate the regular equation of force to solve M_0.

$$M_0 = \frac{F}{4(l_1 + l_2 + R\phi)} \cdot \begin{Bmatrix} 2l_1R\left[\cos(\frac{\pi}{4}+\theta) + \sin(\frac{\pi}{4}+\theta+\phi) - \sin(\frac{\pi}{4}+\theta) - \cos(\frac{\pi}{4}+\theta+\phi) - 2\phi\sin\alpha_1\right] + \\ 2l_2R\left[2\cos(\frac{\pi}{4}+\theta) - 2\cos(\frac{\pi}{4}+\theta+\phi) - \phi\cos\alpha_2 + \phi\sin\alpha_2\right] - \\ l_1^2(\cos\alpha_1 + 3\sin\alpha_1) + l_2^2(3\sin\alpha_2 - \cos\alpha_2) + 2l_1l_2(\sin\alpha_2 - \cos\alpha_2 - 2\sin\alpha_1) + \\ \sqrt{2}R^2\begin{bmatrix} 2\sin\theta + \sqrt{2}\phi\cos(\frac{\pi}{4}+\theta) + \phi\cos\theta - \phi\sin\theta + 2\phi\sin(\theta+\phi) + \\ \cos(\theta+\phi) - \sin(\theta+\phi) - \sqrt{2}\sin(\frac{\pi}{4}+\theta+\phi) \end{bmatrix} \end{Bmatrix} \tag{3}$$

Here, $F = \sigma_x(th/2)$.

The bending moment in the structural beam sections is orderly defined as M_i ($i = 1, 2, \ldots 6$) from J1 to J6, they are expressed as

$$\begin{cases} M_1 = F(x\sin\alpha_1) + M_0, x \in (0, l_1) \\ M_2 = M_1(l_1) + FR\left[\sin(\theta - \dfrac{\pi}{4}) - \sin(\theta + x - \dfrac{\pi}{4})\right], x \in (0, \phi) \\ M_3 = M_2(\phi) - F(x\sin\alpha_2), x \in (0, l_2) \\ M_4 = M_3(l_2) + F(x\cos\alpha_2), x \in (0, l_2) \\ M_5 = M_4(l_2) + FR\left[\sin(\theta + \phi - \dfrac{3\pi}{4}) - \sin(\theta + \phi - \dfrac{3\pi}{4} - x)\right], x \in (0, \phi) \\ M_6 = M_5(\phi) + F(x\cos\alpha_1), x \in (0, l_1) \end{cases} \tag{4}$$

Then, substituting the above bending moments into Eq. (2), the theoretical total strain energy of the unit cell (V_ε^{UC}) is 4 times greater than the quartered cell ($\sum_{i=1}^{6} V_{\varepsilon i}^{QC}$), that is expressed as

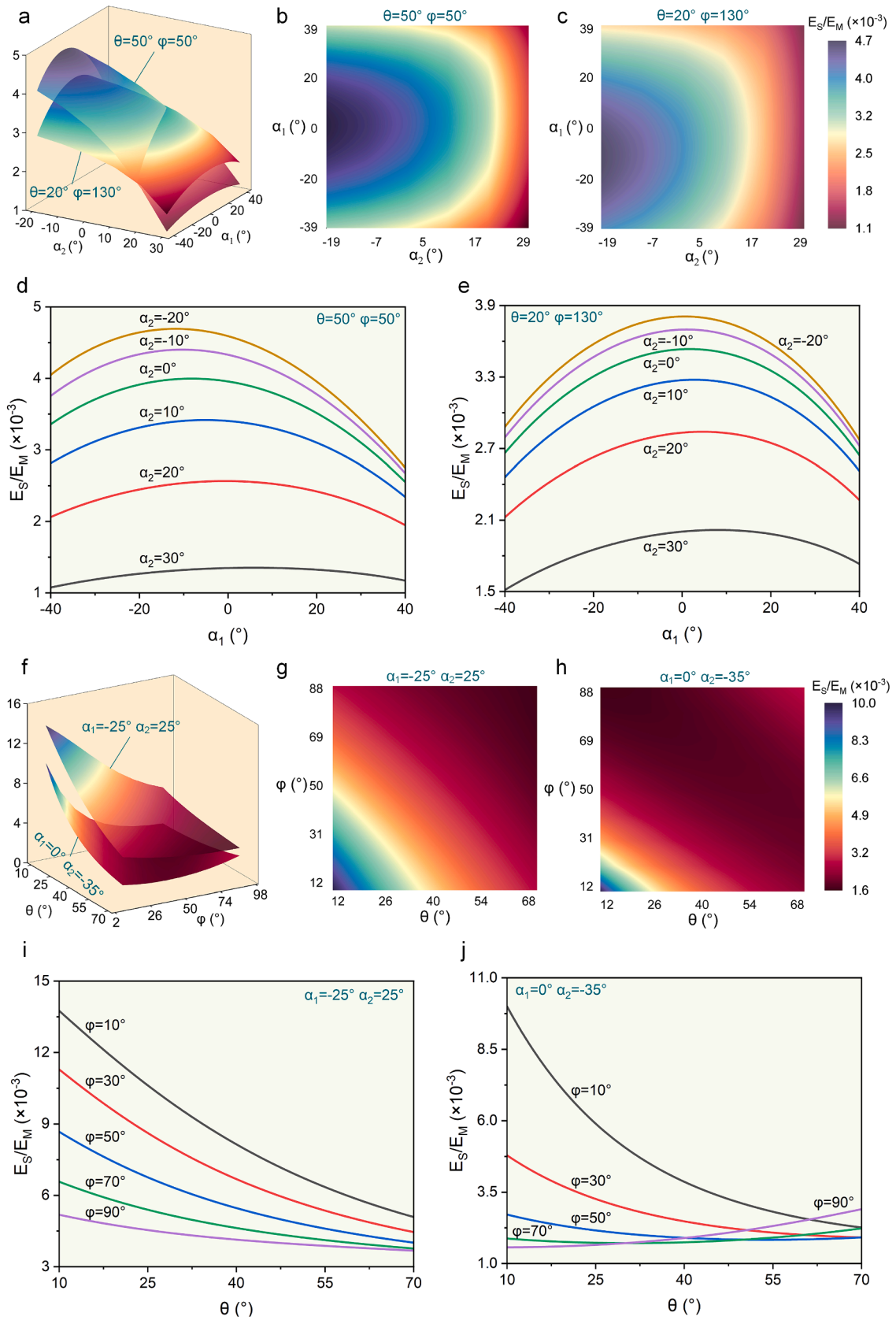

Fig. 2. Plots showing the normalized elastic modulus, structures with $\theta = 50^\circ$ $\varphi = 50^\circ$ and $\theta = 20^\circ$ $\varphi = 130^\circ$: (a) surface of E_S/E_M, (b-c) contour of E_S/E_M, (d and e) curves of E_S/E_M; structures with $\alpha_1 = -25^\circ$ $\alpha_2 = 25^\circ$ and $\alpha_1 = 0^\circ$ $\alpha_2 = -35^\circ$: (f) surface of E_S/E_M, (g and h) contour of E_S/E_M, (i and j) curves of E_S/E_M.

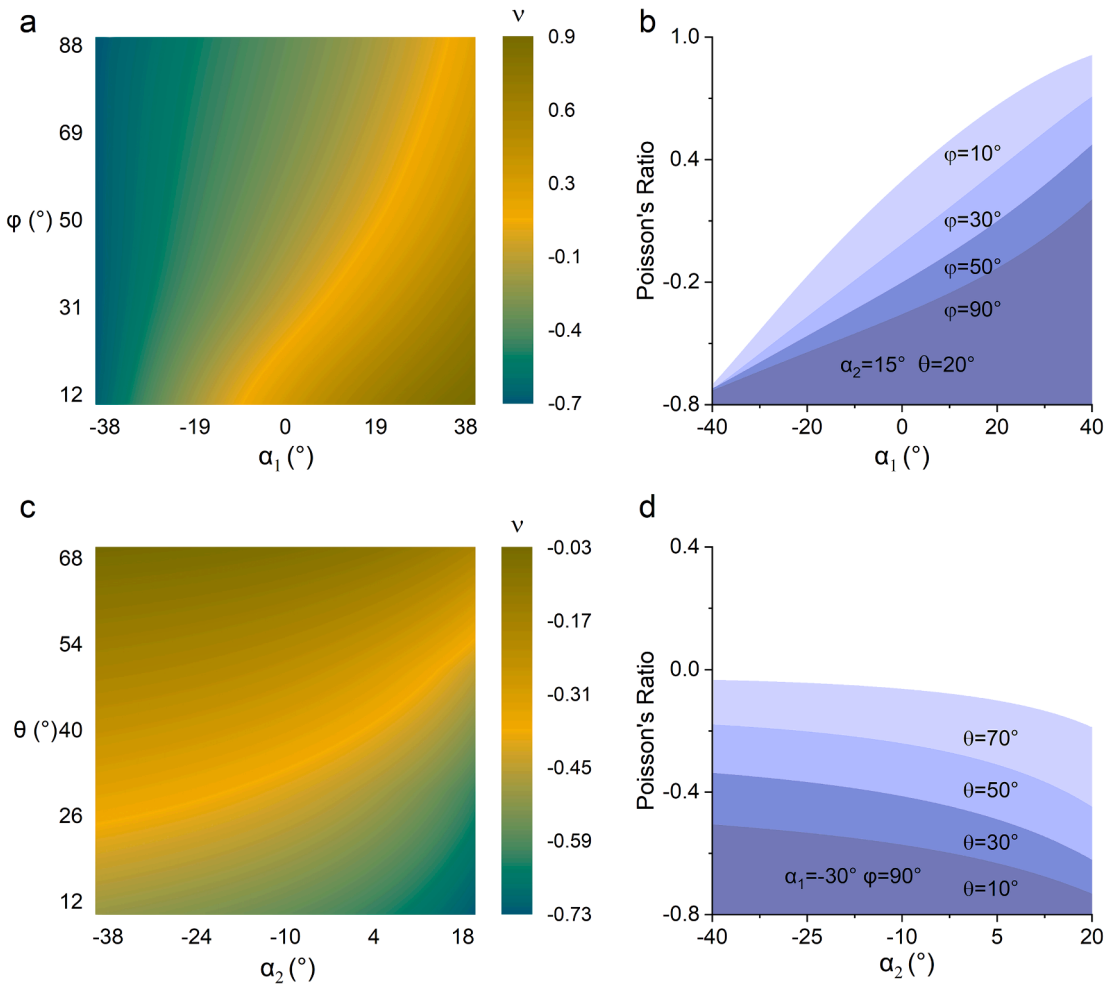

Fig. 3. Plots showing the Poisson's ratio, structures with $\alpha_2 = 15°$ and $\theta = 20°$: (a) contour of ν, (b) curves of ν; structures with $\alpha_1 = 30°$ and $\varphi = 90°$: (c) contour of ν, (d) curves of ν.

$$V_\varepsilon^{UC} = 4\sum_{i=1}^{6} V_{\varepsilon i}^{QC} = 4\sum_{i=1}^{6}\int_{l_i}\frac{M_i^2(x)}{2EI}dx \tag{5}$$

Here, the complete calculation of $V_\varepsilon^{UC} = V_\varepsilon^{UC}(1)+V_\varepsilon^{UC}(2)+V_\varepsilon^{UC}(3)$ is listed as Appendix Eqs. (A1)–(A3).

In this work, the loading direction of the unit cell is its longitudinal direction. When the strain energy V_ε^{UC} is obtained, the unit cell's longitudinal displacement δ_L can be derived from the ratio between the strain energy and generalized force (F). Then the longitudinal strain can be solved by the ratio between longitudinal displacement δ_L and the longitudinal initial dimension L^{UC}. Finally, the theoretical elastic modulus of the proposed mechanical metamaterials can be deduced from the ratio between the normal stress and strain, they are expressed as

$$\begin{cases} \delta_L = \dfrac{V_\varepsilon^{UC}}{F} \\ E^{UC} = \dfrac{\sigma}{\varepsilon_L} = \dfrac{F/(th)}{\delta_L/L^{UC}} \end{cases} \tag{6}$$

3.2. Poisson's ratio

Following the principle of virtual work, the virtual force P is applied at the J7 to solve the perpendicular displacement to the loading direction as illustrated in Fig. 2(b). In this condition, the bending moments in the structural beams are orderly set as M_i'(i = 1, 2, …6), they are expressed as

$$\begin{cases} M_1^{'} = P(x\cos\alpha_1) + F(x\sin\alpha_1) + M_0, x \in (0, l_1) \\ M_2^{'} = PR\left[\cos(\theta - \frac{\pi}{4}) - \cos(\theta + x - \frac{\pi}{4})\right] + \\ FR\left[\sin(\theta - \frac{\pi}{4}) - \sin(\theta + x - \frac{\pi}{4})\right] + M_1^{'}(l_1), x \in (0, \phi) \\ M_3^{'} = P(x\cos\alpha_2) - F(x\sin\alpha_2) + M_2^{'}(\phi), x \in (0, l_2) \\ M_4^{'} = -P(x\sin\alpha_2) + F(x\cos\alpha_2) + M_3^{'}(l_2), x \in (0, l_2) \\ M_5^{'} = PR\left[\cos(\theta + \phi - x - \frac{3\pi}{4}) - \cos(\theta + \phi - \frac{3\pi}{4})\right] + \\ FR\left[\sin(\theta + \phi - \frac{3\pi}{4}) - \sin(\theta + \phi - \frac{3\pi}{4} - x)\right] + M_4^{'}(l_2), x \in (0, \phi) \\ M_6^{'} = P(x\sin\alpha_1) + F(x\cos\alpha_1) + M_5^{'}(\phi), x \in (0, l_1) \end{cases} \tag{7}$$

Then, the transverse displacement δ_T of the unit cell can be solved by employing Castigliano's Second Theorem. Then the theoretical Poisson's ratio ν of the proposed mechanical metamaterials can be obtained from the ratio between the longitudinal strain and transverse strain

$$\begin{cases} \delta_T = \sum_{i=1}^{6}\delta_{Ti} = \sum_{i=1}^{6}\left[\int_{l_i}\dfrac{M_i^{'}(x)}{EI}\dfrac{\partial M_i^{'}(x)}{\partial P}dx\right]_{P=0} \\ \nu = -\dfrac{\varepsilon_T}{\varepsilon_L} = -\dfrac{\delta_T/L_{UC}}{\delta_L/L_{UC}} = -\dfrac{\delta_T}{\delta_L} \end{cases} \tag{8}$$

The complete formulation of $\delta_T = \delta_T(1)+\delta_T(2)$ is listed as Appendix

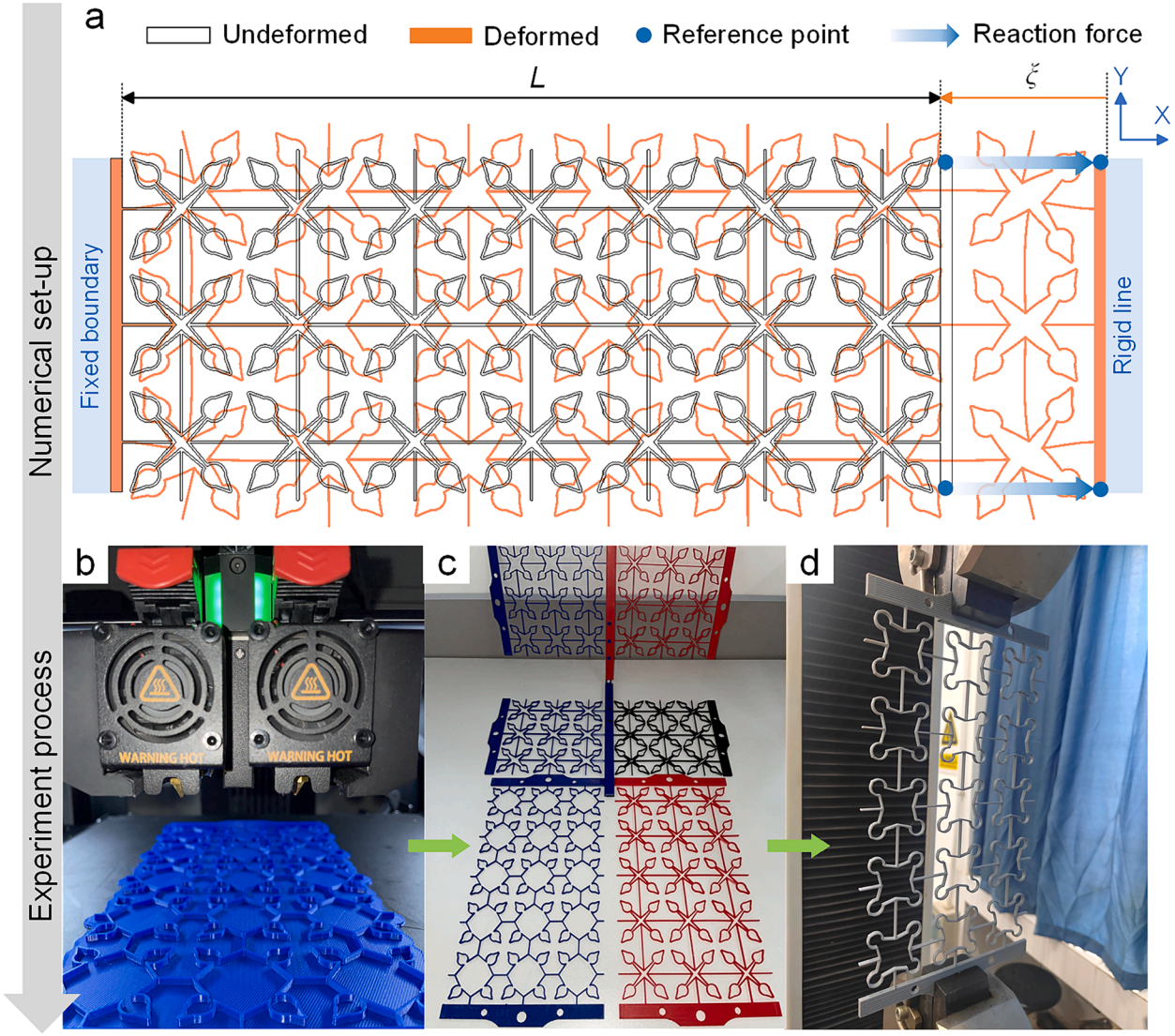

Fig. 4. (a) Numerical simulation set-up, (b–d) samples manufacturing and test.

Eqs. (A4) and (A5).

4. Results and discussion

4.1. Theoretical results

In this section, the theoretical results of equivalent elastic properties of the proposed mechanical metamaterials are presented. To quantitatively study the stiffness of the structures, the normalized effective modulus is obtained from the ratio between the structures' Young's modulus (E_S) and the basic material's Young's modulus (E_M) which is denoted by E_S/E_M, then the effect of the material modulus is effectively excluded. Fig. 2 plots the surfaces and curves of E_S/E_M versus α_1, α_2, θ, and φ. The sub-figures in Fig. 2(a–e) compare the variation of E_S/E_M as the changing α_1 and α_2 when $\theta = 50°$ and $\varphi = 50°$, $\theta = 20°$ and $\varphi = 130°$, respectively. The results show that, α_2 influences E_S/E_M more significantly than α_1.

Further, the α_2 has a greater effect on E_S/E_M for the structures with $\theta = 50°$ and $\varphi = 50°$ than the structures with $\theta = 20°$ and $\varphi = 130°$. Moreover, most of the curves display the shape of a quasi-symmetric arc as the variation of α_1 when $\theta = 20°$ and $\varphi = 130°$. However, the curves $\alpha_2 = -20°$, $-10°$, $0°$, and $10°$ increase at the interval $-40° < \alpha_1 < -10°$ only, then decrease monotonously until $\alpha_1 = 40°$. It can be also observed that the slope of the curves grows slightly with the decreasing α_2. The curves in Fig. 2(d) and (e) indicate the E_S/E_M increases monotonously as the decreases α_2. From Fig. 2(f–j) the results show that the stiffness of the developed flexible mechanical metamaterials can be adjusted by orders of magnitude. The similar phenomenon as Fig. 2(a) can be found in Fig. 2(f), θ influences the E_S/E_M more significantly than φ. As the results in Fig. 2(i), the flexible mechanical metamaterials give the monotonic variation in E_S/E_M, and the significance of θ increases continuously when φ is decreased. It also provides monotonous enlargement in E_S/E_M with decreasing θ.

For the structures with $\alpha_1 = 0°$ and $\alpha_2 = -35°$, the mechanical metamaterials' stiffness follows a similar trend as Fig. 2(i) when $10° < \varphi < 50°$, but provides erratic variation when $50° < \varphi < 90°$. Compared to the sub-figures in Fig. 2, the θ features the most significant influence on E_S/E_M among the four geometric parameters. These findings enable precisely manipulate the stiffness of the devised flexible mechanical metamaterials.

Fig. 3 plots the theoretical results of the Poisson's ratio of the proposed flexible mechanical metamaterials. In Fig. 3(a) and (b), it's readily acquired that for the structures with $\alpha_2 = 15°$ and $\theta = 20°$ the flexible mechanical metamaterials give the continuous reducement in ν when α_1 is decreased or φ is increased. The results show that the Poisson's ratio is widely adjustable from positive to negative. When α_1 nears $-40°$, the

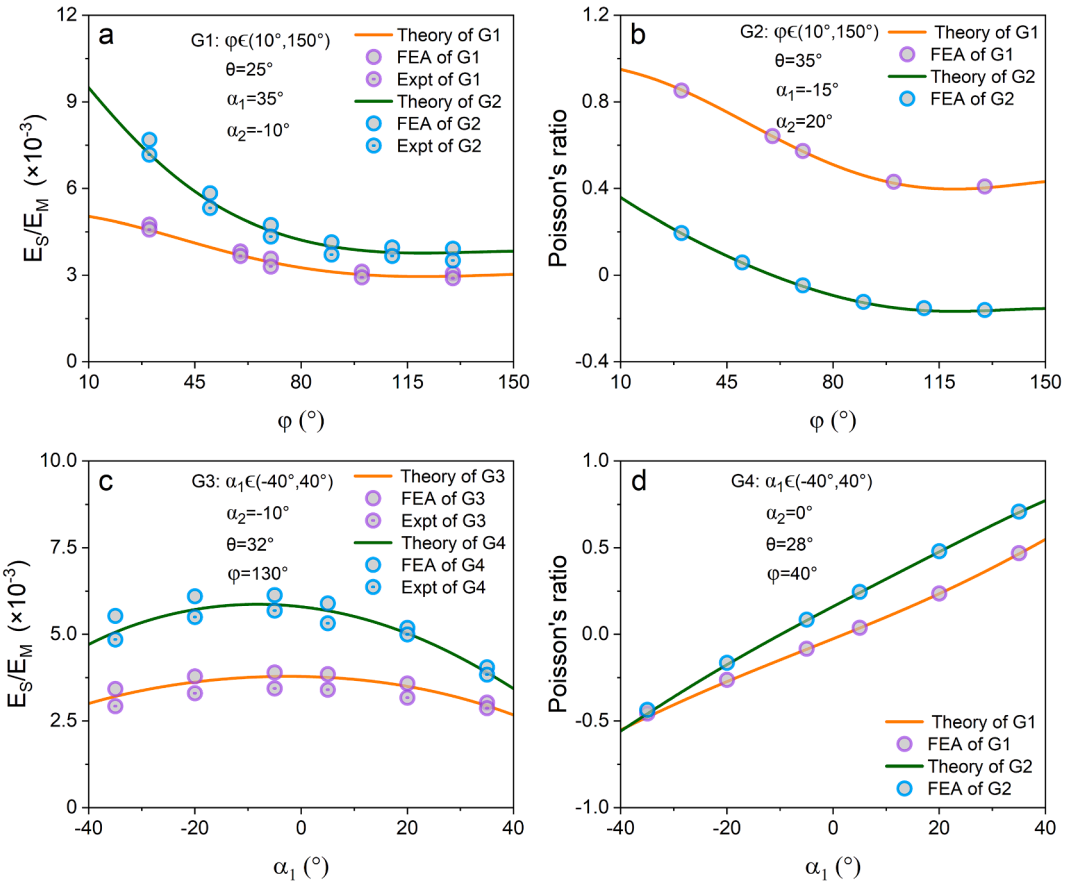

Fig. 5. (a and c) Comparison of different types results of E_S/E_M, (b and d) comparison of different types of results of ν.

variation of φ hardly has any effect on ν.

As observed in Fig. 3(c) and (d), the results demonstrate that for the structures with $\alpha_1 = -30°$ and $\varphi = 90°$ the flexible mechanical metamaterials provide the monotonic reduction in ν when α_2 is grown or θ is decreased. Moreover, for the structures $\alpha_1 = -30°$ $\varphi = 90°$, it's noticeable that the metamaterials remain to feature an auxetic effect when $-40° < \alpha_2 < 20°$ and $10° < \theta < 70°$. This finding is valuable for meeting the specific engineering condition.

4.2. Methodology

The Hyperworks is employed to perform finite element analysis (FEA) static simulation, in order to validate the theoretical results of the elastic constants. The numerical model of the metamaterial is presented in Fig. 4(a). The left end is fixed and the right end is applied axial load, L represents the initial longitudinal dimension of the structures, and ξ represents the longitudinal displacement of the structures, respectively. The numerical model shows that the 4 unit cells at the corner nearly produce rotation and their connecting beams are curved drastically. Fig. 4(b–d) collectively shows the experimental validation process, including the manufacture and the characterization method. All the samples are manufactured by Raise 3D Pro3 Plus with polylactic acid (PLA [74–76]).

The tensile test is achieved by the equipment WDW-100 and the loading speed is 2 mm/min. Fig. 5(a) and (c) compare the theoretical, numerical, and experimental results of the elastic modulus, they suggest that structures in G2 have the highest uniformity in the three types of models. Fig. 5(b) and (d) also demonstrate the excellent accuracy of the theoretical solution, the two types of results agree well.

In Fig. 6, the comparison results on the key mechanical properties between six conventional star-shaped cellular structures (SSCS) and the proposed metamaterials are exhibited. For sample 2, the SSCSs' elastic modulus is 2.8 times greater than the proposed metamaterial as shown in Fig. 6(b). For sample 1–5, the flexible metamaterials' Poisson's ratio is smaller than the SSCS as depicted in Fig. 6(c). The maximum strain is defined as the strain when the structures' VonMises stress is near the yield strength [75,76]. The results show that the flexible metamaterials' maximum strain is considerably greater than the SSCS as seen in Fig. 6 (d). These findings demonstrate that the developed metamaterials perform more sensitive, remarkable auxetic effect, and have higher deformability.

Further, an innovative numerical model is designed by building two layers of flexible mechanical metamaterials composed of 3×3 unit cells as shown in Fig. 7(a), the top and bottom plates are fixed and the middle plate is moved by axial load. The deformation modes of three structures are illustrated in Fig. 7(b), (c), and (d). The structure in Fig. 7(b) features only the longitudinal displacement produced in the two layers, which can be considered as quasi-zero Poisson's ratio.

Moreover, both Fig. 7(c) and (d) exhibit the auxetic effect of the developed mechanical metamaterials. In particular, the numerical model in Fig. 7(d) shows remarkable transverse expansion in the tensile layer and transverse shrinkage in the compression layer. Then, employing the bench clamps, an innovative experiment is designed to verify the feasibility of this phenomenon. Fig. 8(a) shows the experimental apparatus, the two types of flexible metamaterial samples are linked by the connector, fixed by the bench clamps, and the strain is controlled by moving the slider.

In Fig. 8(b), it's readily to observe the experimental and numerical results are highly agreed, sample 1 appears transverse expansion and sample 2 tends to exhibit transverse shrinkage under the longitudinal load. As it turns out, sample1 and sample 2 achieved 13 % strain and sample1 shows the Poisson's ratio near −1 by moving the slider.

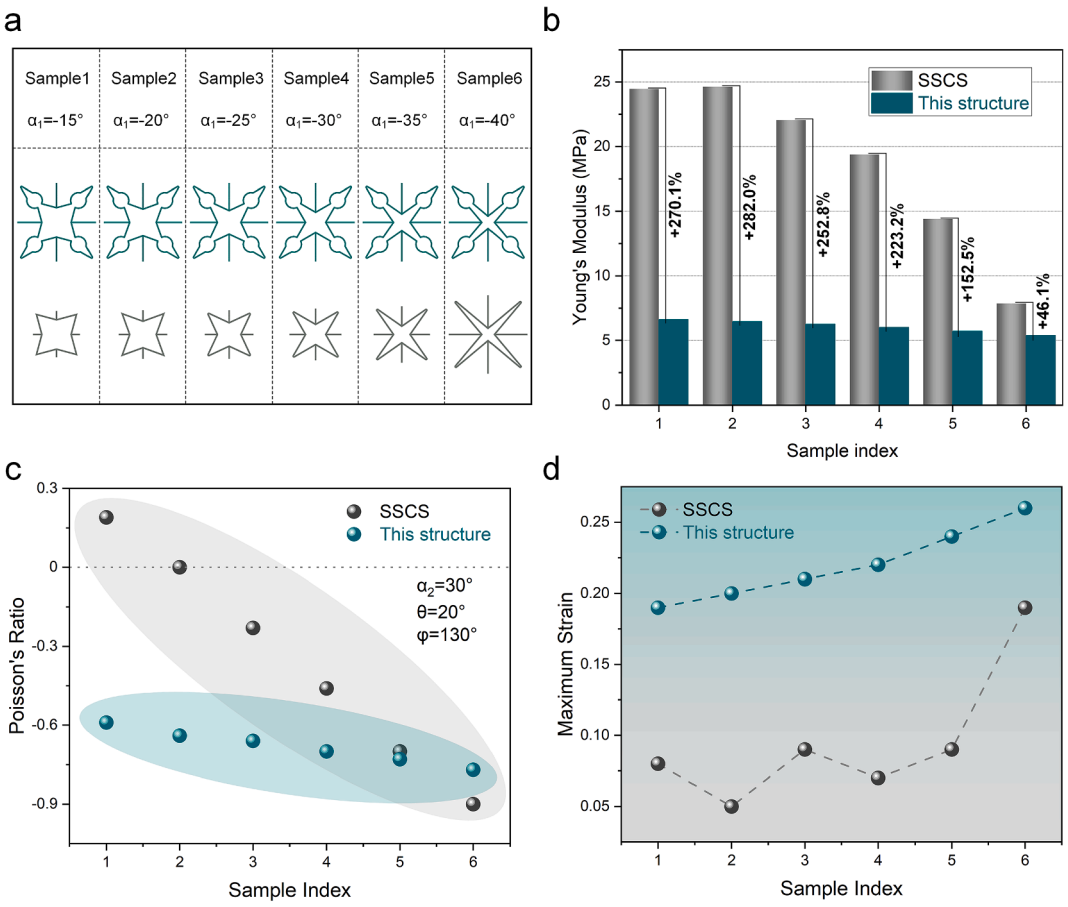

Fig. 6. (a) Six unit cells of the SSCS and the developed structures, (b) comparison on elastic modulus, (c) comparison on Poisson's ratio, and (d) comparison on deformability.

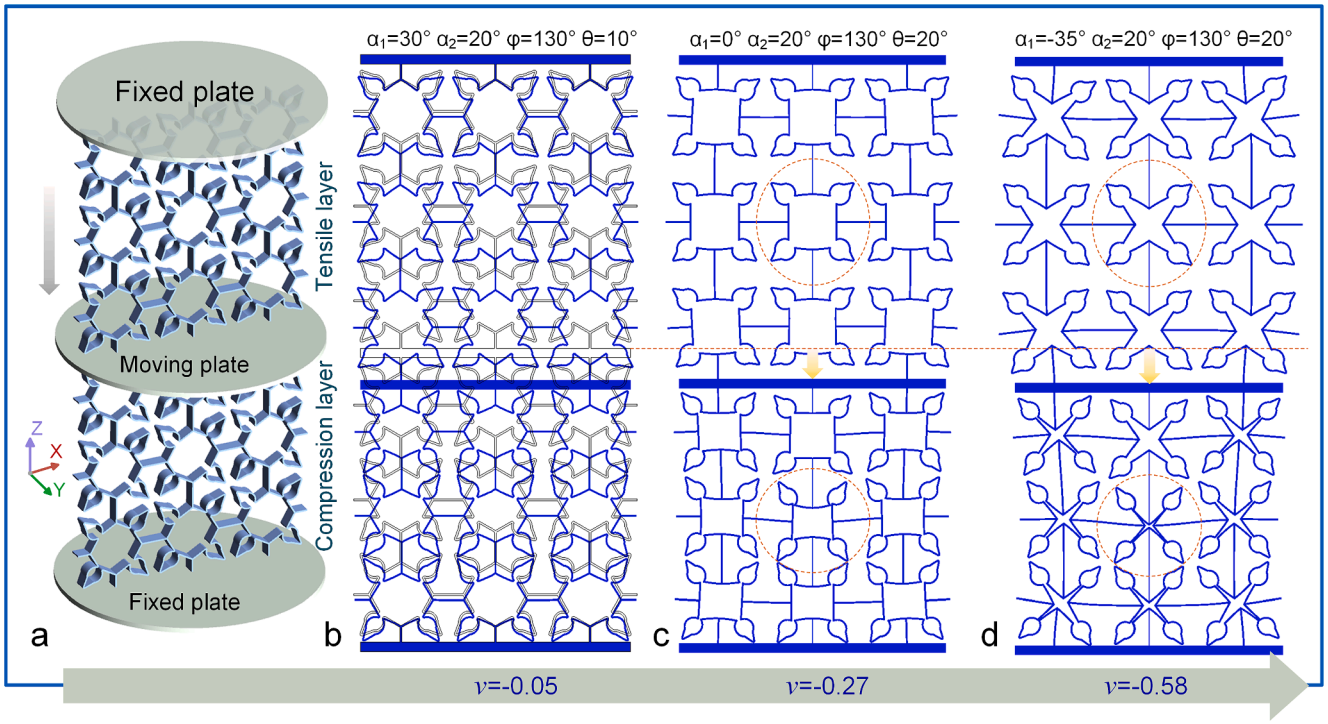

Fig. 7. (a) Schematic of an innovative loading approach, (b-d) the deformation characteristics of different structures.

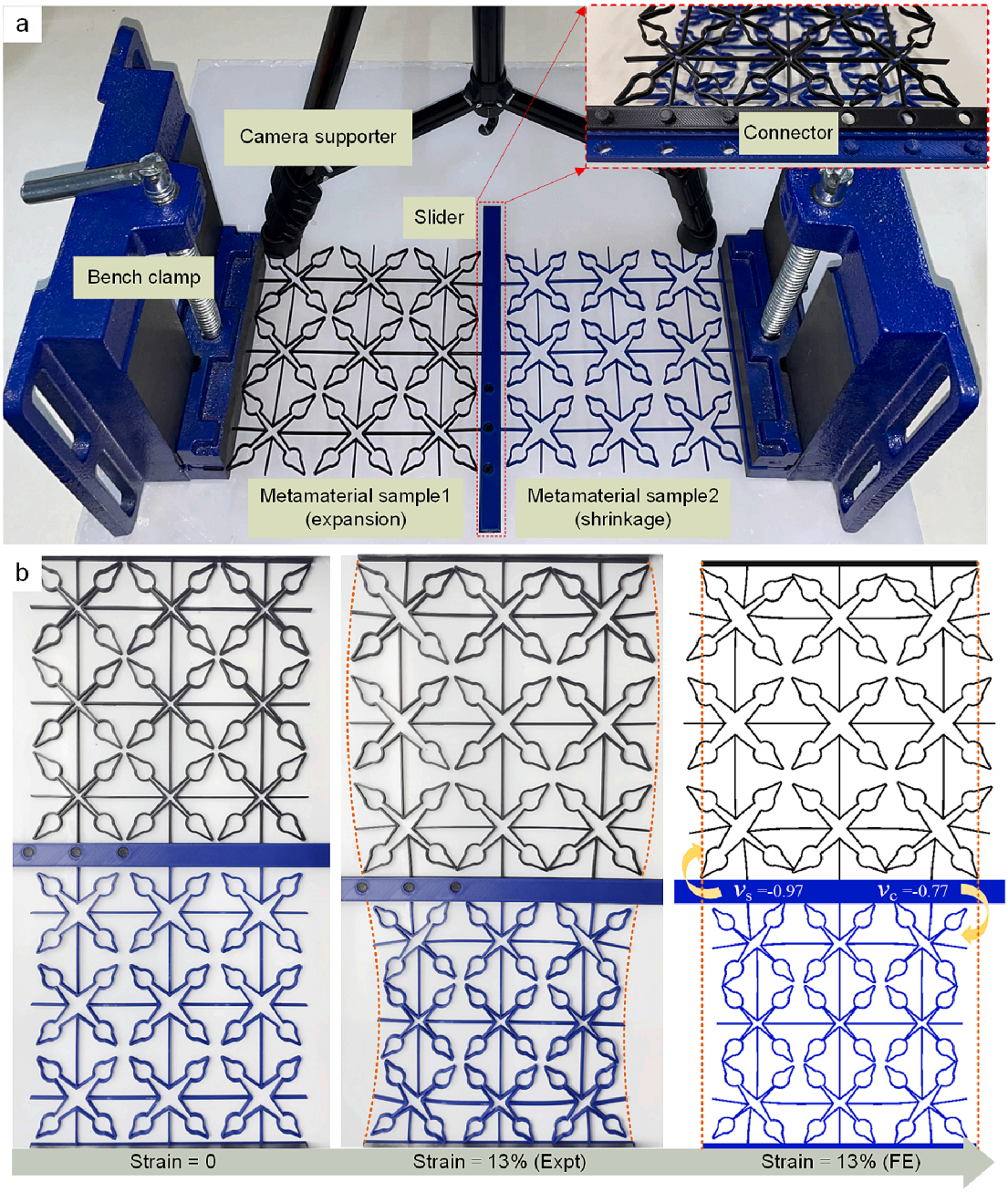

Fig. 8. (a) Experiment layout for validating the phenomenon of structure's synchronous expansion and shrinkage, (b) comparison of experimental and numerical deformation.

A simple coupling system employing the developed flexible metamaterials is designed in this section. The device is composed of two types of flexible mechanical metamaterials and a slideable state switch which is used to transform the two states of the device, as presented in Fig. 9(a). Fig. 9(b) illustrates the different auxetic cellular structures, which also potential to induce the metamaterials system's profile occurring the wavy deformation. In Fig. 9(c), and the similar concept was successfully implemented on the arc-shaped metamaterial.

5. Conclusion

The mechanical properties of flexible mechanical metamaterials manufactured from polylactic acid are theoretically studied via the energy principle and Castigliano's second theorem, validated experimentally complemented with numerical simulation. The metamaterials with multifarious configurations were manufactured by 3D printing in the form of flexible board. According to a complete parametric study, the geometric parameters of the metamaterials were demonstrated to significantly influence their mechanical response. This work disclosed

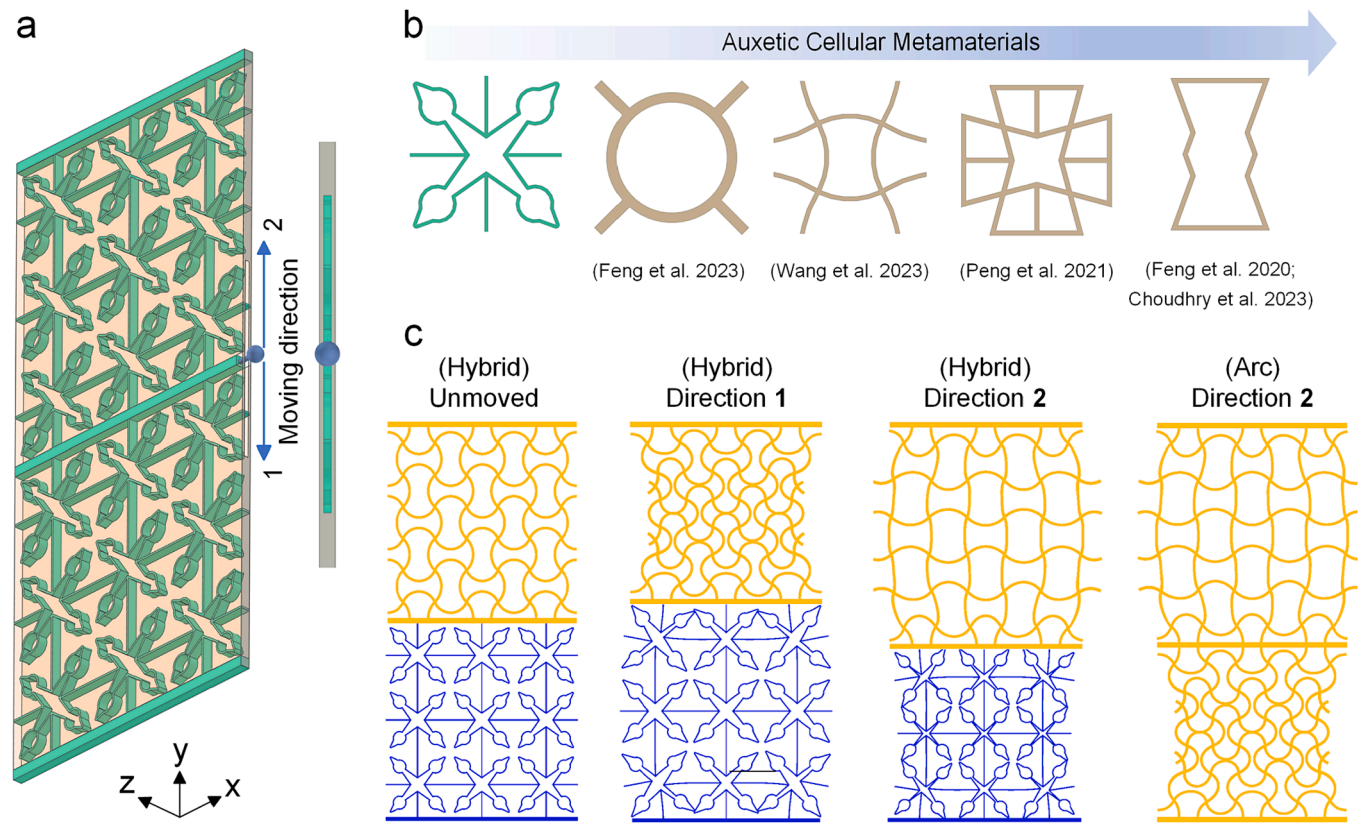

Fig. 9. (a) Schematic of the devised wave-induceable incorporating device, (b) multifarious planar auxetic metamaterials [52,77–80], (c) the wavy deformation achieved by hybrid metamaterials and single arc-shaped metamaterials.

the relationship between these phenomena and the deformation mechanisms occurring at the individual unit cells. The normalized elastic modulus of the structures can be adjusted from 1 to 13.6 ($\times 10^{-3}$), and their Poisson's ratio can be tailored from −1 to 1. Moreover, the wavy deformation was achieved by coupling the developed metamaterials to a system, this concept was successfully implemented for other metamaterials. Multidimensional mechanical properties between the developed metamaterials and the star-shaped cellular structures are compared, and the results demonstrated the developed flexible mechanical metamaterials are more sensitive, auxetic, and deformable. The potential use of the proposed flexible metamaterials was revealed by the design, fabrication, and test of a coupling system with two structures, showing a Poisson's ratio of near −1 and 13 % strain. Finally, the developed coupling design provided a valid way to induce the metamaterials system's profile occurring the wavy deformation.

CRediT authorship contribution statement

Shangbin Wang: Writing – original draft, Visualization, Validation, Supervision, Software, Methodology, Investigation, Data curation, Conceptualization. **Junxian Guo:** Writing – review & editing, Resources, Methodology, Funding acquisition, Conceptualization. **Andras Biczo:** Writing – review & editing, Supervision, Methodology, Conceptualization. **Ning Feng:** Writing – review & editing, Supervision, Methodology, Conceptualization.

Declaration of competing interest

The authors declare that they have no known competing financial interests or personal relationships that could have appeared to influence the work reported in this paper.

Data availability

All data, models, and code generated or used during the study appear in the submitted paper.

Acknowledgements

This research is supported by the Project of science and technology innovation team (Tianshan innovation team) and Xinjiang smart agricultural information perception technology innovation (2022TSYCTD0011).

Appendix

$$V_{\varepsilon}^{UC}(1)=\frac{F^2R^2}{EI}\left\{\begin{array}{l} R\left[\begin{array}{c} -\frac{\phi}{2}\sin2\theta+\frac{1}{2}\sin(2\theta+2\phi)+\frac{1}{2}\cos2\theta-\sin(2\theta+\phi)-\sin\phi- \\ \cos(2\theta+\phi)+\frac{3\phi}{2}-1+\frac{1}{2}\cos(2\theta+2\phi)-\frac{\phi}{2}\cos\phi+\frac{\phi}{2}\cos(2\theta+\phi) \\ -\frac{\phi}{2}\cos(2\theta+2\phi)+\cos\phi+\frac{1}{2}\sin2\theta+\frac{\phi}{2}\sin(2\theta+\phi)+\frac{\phi}{2}\sin\theta \end{array}\right]+ \\ L_2\left[\begin{array}{c} -\frac{1}{2}\sin(2\theta+2\phi)-\frac{\sqrt{2}}{2}\sin(\alpha_2+\theta)-\frac{1}{2}\sin2\theta-\frac{\sqrt{2}}{2}\phi\sin(\theta+\phi+\alpha_2)+ \\ \sin(2\theta+\phi)+\frac{\sqrt{2}}{2}\cos(\alpha_2-\theta)-\frac{\sqrt{2}}{2}\phi\cos(\alpha_2-\theta)+\frac{\sqrt{2}}{2}\sin(\theta+\phi+\alpha_2)+ \\ \frac{\sqrt{2}}{2}\phi\sin(\alpha_2+\theta)-\cos\phi-\frac{\sqrt{2}}{2}\cos(-\theta-\phi+\alpha_2)-\frac{\sqrt{2}}{2}\phi\cos(\alpha_2+\theta+\phi) \\ +\frac{\sqrt{2}}{2}\phi\cos(\alpha_2-\theta-\phi)+\frac{\sqrt{2}}{2}\phi\sin(\alpha_2-\theta-\phi)+1 \end{array}\right]+ \\ L_2\left[\begin{array}{c} 1-\cos\phi-\frac{1}{2}\cos(2\theta+2\phi)-\frac{1}{2}\cos2\theta+\cos(2\theta+\phi)+\frac{\sqrt{2}}{2}\cos(\alpha_1+\theta)- \\ \frac{\sqrt{2}}{2}\cos(\alpha_1-\theta)-\frac{\sqrt{2}}{2}\phi\cos(\alpha_1-\theta-\phi)+\frac{\sqrt{2}}{2}\phi\cos(\alpha_1+\theta+\phi)+ \\ \frac{\sqrt{2}}{4}\theta\cos(\alpha_1+\theta)-\frac{\sqrt{2}}{4}\phi\sin(\alpha_1+\theta)+\frac{\sqrt{2}}{4}\theta\sin(\alpha_1+\theta)-\frac{\sqrt{2}}{4}\phi\cos(\alpha_1+\theta) \\ +\frac{1}{2}\sin(\alpha_1-\theta-\phi+\frac{\pi}{4})+\frac{\sqrt{2}}{4}\cos(\alpha_1-\theta-\phi)-\frac{\phi}{2}\sin(\alpha_1+\theta+\frac{\pi}{4})+ \\ \frac{\theta}{2}\cos(\alpha_1-\theta+\frac{\pi}{4})+\frac{\pi}{8}\cos(\alpha_1-\theta+\frac{\pi}{4})-\frac{\sqrt{2}}{4}\sin(\alpha_1+\theta+\frac{\pi}{4})- \\ \frac{\sqrt{2}}{4}\theta\cos(\alpha_1-\theta)+\frac{\sqrt{2}}{4}\theta\sin(\alpha_1-\theta)+\frac{\sqrt{2}}{4}\phi\cos(\alpha_1-\theta)+\frac{\phi}{2}\cos(\alpha_1-\theta+\frac{\pi}{4}) \\ +\frac{\sqrt{2}}{16}\pi\cos(\alpha_1+\theta)-\frac{\sqrt{2}}{4}\phi\sin(\alpha_1-\theta)+\frac{\sqrt{2}}{16}\pi\sin(\alpha_1-\theta)+\frac{\sqrt{2}}{16}\pi\sin(\alpha_1+\theta) \\ -\frac{\sqrt{2}}{16}\pi\cos(\alpha_1-\theta)-\frac{\pi}{8}\sin(\alpha_1+\theta+\frac{\pi}{4})-\frac{1}{2}\cos(\alpha_1+\theta+\phi+\frac{\pi}{4})- \\ \frac{\theta}{2}\sin(\alpha_1+\theta+\frac{\pi}{4})-\frac{\sqrt{2}}{4}\sin(\alpha_1-\theta-\phi)-\frac{\sqrt{2}}{4}\cos(\alpha_1+\theta+\phi) \end{array}\right] \end{array}\right\} \tag{A1}$$

$$V_{\varepsilon}^{UC}(2)=\frac{FM_0}{EI}\left\{\begin{array}{l} RL_2\left[2\phi\cos\alpha_2+4\cos(\theta+\phi+\frac{\pi}{4})-2\phi\sin\alpha_2-4\cos(\theta+\frac{\pi}{4})\right]+ \\ RL_1\left[\begin{array}{c} 2\sin(\theta+\frac{\pi}{4})+2\cos(\theta+\phi+\frac{\pi}{4})-2\sin(\theta+\phi+\frac{\pi}{4})+ \\ 4\phi\sin\alpha_1-2\cos(\theta+\frac{\pi}{4}) \end{array}\right]+ \\ L_2^2(\cos\alpha_2-3\sin\alpha_2)+4(R\phi+L_2+L_1)+ \\ L_1^2(\cos\alpha_1+3\sin\alpha_1)+ \\ L_1L_2(2\cos\alpha_2-2\sin\alpha_2+4\sin\alpha_1)+ \\ R^2\left[\begin{array}{c} 2\sin(\theta+\phi+\frac{\pi}{4})+\sqrt{2}\sin(\theta+\phi)-2\sqrt{2}\sin\theta+\sqrt{2}\theta\cos\theta+\sqrt{2}\phi\sin\theta- \\ \sqrt{2}\phi\cos\theta+\sqrt{2}\ \frac{\pi}{4}\cos\theta-\sqrt{2}\ \frac{\pi}{4}\sin\theta-2\sqrt{2}\phi\sin(\theta+\phi)-\frac{\pi}{2}\cos(\theta+\frac{\pi}{4}) \\ -\sqrt{2}\theta\sin\theta-\sqrt{2}\cos(\theta+\phi)-2\phi\cos(\theta+\frac{\pi}{4})-2\theta\cos(\theta+\frac{\pi}{4}) \end{array}\right] \end{array}\right\} \tag{A2}$$

$$V_{\varepsilon}^{UC}(3)=\frac{F^2}{EI}\left\{\begin{array}{c} L_2^3(-\frac{1}{4}\cos 2\alpha_2+\frac{5}{12}-\frac{1}{4}\sin 2\alpha_2)+L_1^3(\frac{5}{12}+\frac{1}{4}\sin 2\alpha_1-\frac{1}{4}\cos 2\alpha_1)+ \\ L_1^2L_2\left[\begin{array}{c} -\frac{3}{4}\sin(\alpha_2-\alpha_1)+\frac{1}{2}+\frac{1}{4}\sin(\alpha_2+\alpha_1)- \\ \frac{1}{4}\cos(\alpha_2-\alpha_1)+\frac{3}{4}\cos(\alpha_2+\alpha_1)-\frac{1}{2}\cos 2\alpha_1 \end{array}\right]+ \\ L_2^2L_1\left[\begin{array}{c} -\frac{3}{4}\cos(\alpha_2-\alpha_1)+\frac{1}{2}+\frac{1}{4}\sin(\alpha_2+\alpha_1)+ \\ \frac{3}{4}\cos(\alpha_2+\alpha_1)-\frac{1}{4}\sin(\alpha_2-\alpha_1)-\frac{1}{2}\sin 2\alpha_2 \end{array}\right]+ \\ RL_1L_2\left[\begin{array}{c} -\sin(\alpha_2+\theta+\phi+\frac{\pi}{4})-\sin(\alpha_1+\theta+\frac{\pi}{4})+\sin(\alpha_2-\theta-\phi+\frac{\pi}{4}) \\ +\frac{\phi}{2}\sin(\alpha_2+\alpha_1)+\frac{\phi}{2}\cos(\alpha_2+\alpha_1)+\sin(\alpha_1+\theta+\phi+\frac{\pi}{4})+ \\ \sin(\alpha_2+\theta+\frac{\pi}{4})-\sin(\alpha_2-\theta+\frac{\pi}{4})+\cos(\alpha_1-\theta+\frac{\pi}{4})- \\ \frac{\phi}{2}\cos(\alpha_2-\alpha_1)-\cos(\alpha_1-\theta-\phi+\frac{\pi}{4})-\frac{\phi}{2}\sin(\alpha_2-\alpha_1) \end{array}\right]+ \\ RL_1^2\left[\begin{array}{c} -\frac{4}{3}\cos(\alpha_1+\theta+\frac{\pi}{4})-\frac{1}{4}\sin(\alpha_1+\theta+\frac{\pi}{4})+\frac{1}{4}\sin(\alpha_1-\theta+\frac{\pi}{4})+\frac{\phi}{2}- \\ \frac{3}{4}\cos(\alpha_1-\theta-\phi+\frac{\pi}{4})+\frac{3}{4}\cos(\alpha_1-\theta+\frac{\pi}{4})+\frac{3}{4}\cos(\alpha_1+\theta+\phi+\frac{\pi}{4}) \\ -\frac{\phi}{2}\cos 2\alpha_1+\frac{1}{4}\sin(\alpha_1+\theta+\phi+\frac{\pi}{4})-\frac{1}{4}\sin(\alpha_1-\theta-\phi+\frac{\pi}{4}) \end{array}\right]+ \\ RL_2^2\left[\begin{array}{c} \frac{1}{4}\sin(\alpha_2-\theta-\phi+\frac{\pi}{4})+\frac{3}{4}\sin(\alpha_2+\theta+\frac{\pi}{4})-\frac{3}{4}\cos(\alpha_2-\theta+\frac{\pi}{4}) \\ -\frac{1}{4}\sin(\alpha_2-\theta+\frac{\pi}{4})-\frac{1}{4}\cos(\alpha_2+\theta+\frac{\pi}{4})+\frac{\phi}{2}+\frac{1}{4}\cos(\alpha_2+\theta+\phi+\frac{\pi}{4}) \\ -\frac{\phi}{2}\sin 2\alpha_2-\frac{3}{4}\sin(\alpha_2+\theta+\phi+\frac{\pi}{4})+\frac{3}{4}\cos(\alpha_2-\theta-\phi+\frac{\pi}{4}) \end{array}\right] \end{array}\right\} \tag{A3}$$

$$\delta_T(1)=\frac{1}{24EI}\left\{\begin{array}{c} M_0R^2\left[\begin{array}{c}-24\sqrt{2}\cos(\theta+\phi)-6\sqrt{2}\,\pi\cos\theta-24\sqrt{2}\sin(\theta+\phi)+48\phi\sin(\theta+\frac{\pi}{4})-24\sqrt{2}\,\theta\sin\theta\\ -24\sqrt{2}\,\theta\cos\theta+48\cos(\theta+\phi+\frac{\pi}{4})+24\sqrt{2}\,\phi\cos\theta+24\sqrt{2}\,\phi\sin\theta-6\sqrt{2}\,\pi\sin\theta\\ +48\theta\sin(\theta+\frac{\pi}{4})-48\sqrt{2}\,\phi\sin(\theta+\phi)+12\pi\sin(\theta+\frac{\pi}{4})+48\sqrt{2}\sin\theta\end{array}\right]+\\ M_0L_2^2(72\cos\alpha_2-24\sin\alpha_2)+M_0L_1^2[72\cos\alpha_1+24\sin\alpha_1]+\\ M_0L_1L_2[48\cos\alpha_2+96\cos\alpha_1-48\sin\alpha_2]+\\ M_0L_2\left[48\phi\cos\alpha_2-96\sin(\theta+\phi+\frac{\pi}{4})-48\phi\sin\alpha_2+96\sin(\theta+\frac{\pi}{4})\right]+\\ M_0L_1R\left[\begin{array}{c}96\phi\cos\alpha_1+48\cos(\theta+\phi+\frac{\pi}{4})-48\cos(\theta+\frac{\pi}{4})-\\ 48\sin(\theta+\phi+\frac{\pi}{4})+48\sin(\theta+\frac{\pi}{4})\end{array}\right]+\\ FR^3\left[\begin{array}{c}24\phi-24\phi\cos(2\theta+2\phi)-24\phi\cos2\theta+24\phi\cos(2\theta+\phi)-\\ 24\phi\cos\phi-12\sin2\theta+12\sin(2\theta+2\phi)\end{array}\right]+\\ FR^2L_2\left[\begin{array}{c}12\sqrt{2}\,\phi\cos(\alpha_2+\theta)-12\sqrt{2}\,\phi\cos(\alpha_2-\theta)-12\sqrt{2}\,\phi\sin(\alpha_2-\theta)-\\ 12\sqrt{2}\sin(\alpha_2+\theta)-12\sqrt{2}\sin(\alpha_2-\theta)-24\sqrt{2}\,\phi\sin(\alpha_2+\theta+\phi)+\\ 24\sqrt{2}\,\phi\sin(\alpha_2-\theta-\phi)-24\cos(2\theta+2\phi)+12\sqrt{2}\sin(\alpha_2-\theta-\phi)+\\ 12\sqrt{2}\cos(\alpha_2-\theta)+12\sqrt{2}\cos(\alpha_2+\theta)-24\sqrt{2}\,\phi\cos(\alpha_2+\theta+\phi)+\\ 12\sqrt{2}\,\phi\sin(\alpha_2+\theta)+24\sqrt{2}\,\phi\cos(\alpha_2-\theta-\phi)-12\sqrt{2}\cos(\alpha_2-\theta-\phi)+\\ 48\cos(2\theta+\phi)-24\cos2\theta-12\sqrt{2}\cos(\alpha_2+\theta+\phi)+12\sqrt{2}\sin(\alpha_2+\theta+\phi)\end{array}\right]+\\ FR^2L_1\left[\begin{array}{c}-3\sqrt{2}\,\pi\sin(\alpha_1+\theta)-24\cos(2\theta+2\phi)-24\cos2\theta+48\cos(2\theta+\phi)-\\ 12\sqrt{2}\cos(\alpha_1+\theta)+12\sqrt{2}\cos(\alpha_1-\theta)-12\sqrt{2}\,\phi\cos(\alpha_1-\theta-\phi)+\\ 12\sqrt{2}\,\phi\cos(\alpha_1+\theta+\phi)+12\sqrt{2}\,\theta\cos(\alpha_1+\theta)+12\sqrt{2}\,\phi\sin(\alpha_1+\theta)+\\ 3\sqrt{2}\,\pi\cos(\alpha_1+\theta)+48-12\sqrt{2}\,\theta\sin(\alpha_1+\theta)+12\sqrt{2}\,\phi\sin(\alpha_1-\theta-\phi)\\ -12\sqrt{2}\,\phi\sin(\alpha_1+\theta+\phi)-12\sqrt{2}\,\phi\cos(\alpha_1+\theta)-12\sqrt{2}\cos(\alpha_1-\theta-\phi)\\ -24\theta\cos(\alpha_1+\frac{\pi}{4}+\theta)-24\phi\cos(\alpha_1+\frac{\pi}{4}+\theta)-6\pi\cos(\alpha_1+\frac{\pi}{4}+\theta)+\\ 12\sqrt{2}\sin(\alpha_1-\theta)-48\cos\phi-12\sqrt{2}\sin(\alpha_1+\theta)+24\sin(\alpha_1+\theta+\phi+\frac{\pi}{4})\\ -12\sqrt{2}\sin(\alpha_1-\theta-\phi)\end{array}\right]\end{array}\right\} \tag{A4}$$

$$\delta_T(2)=\frac{F}{24EI}\left\{\begin{array}{c} L_1L_2^2[24-36\sin(\alpha_2-\alpha_1)-24\sin2\alpha_2+12\cos(\alpha_2+\alpha_1)]+\\ L_1^2L_2[36\cos(\alpha_2+\alpha_1)-36\sin(\alpha_2-\alpha_1)+24\sin2\alpha_1]+\\ RL_1L_2\left[\begin{array}{c}-24\phi\sin(\alpha_2-\alpha_1)-48\sin(\alpha_2+\frac{\pi}{4}+\theta+\phi)+24\phi\cos(\alpha_2+\alpha_1)+48\sin(\alpha_2+\frac{\pi}{4}+\theta)-\\ 48\cos(\alpha_1+\frac{\pi}{4}+\theta)+48\sin(\alpha_2+\frac{\pi}{4}-\theta-\phi)-48\sin(\alpha_2+\frac{\pi}{4}-\theta)+48\cos(\alpha_1+\frac{\pi}{4}+\theta+\phi)\end{array}\right]+\\ RL_2^2\left[\begin{array}{c}12\sin(\alpha_2+\frac{\pi}{4}+\theta)+36\sin(\alpha_2+\frac{\pi}{4}-\theta-\phi)-24\phi\sin2\alpha_2-\\ 12\sin(\alpha_2+\frac{\pi}{4}+\theta+\phi)-36\sin(\alpha_2+\frac{\pi}{4}-\theta)+24\phi\end{array}\right]+\\ RL_1^2\left[\begin{array}{c}-36\cos(\alpha_1+\frac{\pi}{4}-\theta-\phi)-36\cos(\alpha_1+\frac{\pi}{4}+\theta)+36\cos(\alpha_1+\frac{\pi}{4}-\theta)\\ +36\cos(\alpha_1+\frac{\pi}{4}+\theta+\phi)+24\phi\sin2\alpha_1\end{array}\right]+\\ L_1^3(20\sin2\alpha_1+12)+L_2^3(12-20\sin2\alpha_2)\end{array}\right\} \tag{A5}$$

References

[1] K. Bertoldi, V. Vitelli, J. Christensen, M. Van Hecke, Flexible mechanical metamaterials, Nat. Rev. Mater. 2 (11) (2017) 1–11.
[2] J.U. Surjadi, L. Gao, H. Du, X. Li, X. Xiong, N.X. Fang, Y. Lu, Mechanical metamaterials and their engineering applications, Adv. Eng. Mater. 21 (3) (2019) 1800864.
[3] B. Florijn, C. Coulais, M. van Hecke, Programmable mechanical metamaterials, Phys. Rev. Lett. 113 (17) (2014) 175503.
[4] X. Zheng, H. Lee, T.H. Weisgraber, M. Shusteff, J. DeOtte, E.B. Duoss, J.D. Kuntz, M.M. Biener, Q. Ge, J.A. Jackson, Ultralight, ultrastiff mechanical metamaterials, Science 344 (6190) (2014) 1373–1377.
[5] P. Jiao, J. Mueller, J.R. Raney, X. Zheng, A.H. Alavi, Mechanical metamaterials and beyond, Nat. Commun. 14 (1) (2023) 6004.
[6] C. Coulais, E. Teomy, K. De Reus, Y. Shokef, M. Van Hecke, Combinatorial design of textured mechanical metamaterials, Nature 535 (7613) (2016) 529–532.
[7] J.L. Silverberg, A.A. Evans, L. McLeod, R.C. Hayward, T. Hull, C.D. Santangelo, I. Cohen, Using origami design principles to fold reprogrammable mechanical metamaterials, Science 345 (6197) (2014) 647–650.
[8] X. Fang, J. Wen, L. Cheng, D. Yu, H. Zhang, P. Gumbsch, Programmable gear-based mechanical metamaterials, Nat. Mater. 21 (8) (2022) 869–876.
[9] Z. Vangelatos, K. Komvopoulos, C. Grigoropoulos, Vacancies for controlling the behavior of microstructured three-dimensional mechanical metamaterials, Math. Mech. Solids 24 (2) (2019) 511–524.
[10] P. Jiao, A.H. Alavi, Artificial intelligence-enabled smart mechanical metamaterials: advent and future trends, Int. Mater. Rev. 66 (6) (2021) 365–393.
[11] R. Hedayati, A. Güven, S. Van der Zwaag, 3D gradient auxetic soft mechanical metamaterials fabricated by additive manufacturing, Appl. Phys. Lett. 118 (14) (2021).
[12] M. Bodaghi, W. Liao, 4D printed tunable mechanical metamaterials with shape memory operations, Smart Mater. Struct. 28 (4) (2019) 045019.
[13] X. Zhou, L. Ren, Z. Song, G. Li, J. Zhang, B. Li, Q. Wu, W. Li, L. Ren, Q. Liu, Advances in 3D/4D printing of mechanical metamaterials: from manufacturing to applications, Compos. B Eng. (2023) 110585.
[14] H.M. Kolken, A. Zadpoor, Auxetic mechanical metamaterials, RSC Adv. 7 (9) (2017) 5111–5129.
[15] K.K. Dudek, J.A.I. Martínez, G. Ulliac, M. Kadic, Micro-scale auxetic hierarchical mechanical metamaterials for shape morphing, Adv. Mater. 34 (14) (2022) 2110115.
[16] X. Li, W. Peng, W. Wu, J. Xiong, Y. Lu, Auxetic mechanical metamaterials: from soft to stiff, Int. J. Extreme Manuf. 5 (4) (2023) 042003.
[17] A. Sorrentino, D. Castagnetti, L. Mizzi, A. Spaggiari, Bio-inspired auxetic mechanical metamaterials evolved from rotating squares unit, Mech. Mater. 173 (2022) 104421.
[18] J. Zhang, G. Lu, Z. You, Large deformation and energy absorption of additively manufactured auxetic materials and structures: a review, Compos. B Eng. 201 (2020) 108340.
[19] R.P. Bohara, S. Linforth, T. Nguyen, A. Ghazlan, T. Ngo, Anti-blast and-impact performances of auxetic structures: a review of structures, materials, methods, and fabrications, Eng. Struct. 276 (2023) 115377.
[20] X. Zhu, J. Zhang, W. Zhang, J. Chen, Vibration frequencies and energies of an auxetic honeycomb sandwich plate, Mech. Adv. Mater. Struct. 26 (23) (2019) 1951–1957.
[21] M.B. Francisco, J.L.J. Pereira, G.A. Oliver, L.R. Roque da Silva, S.S. Cunha Jr, G. F. Gomes, A review on the energy absorption response and structural applications of auxetic structures, Mech. Adv. Mater. Struct. 29 (27) (2022) 5823–5842.
[22] F. La Malfa, S. Puce, F. Rizzi, M. De Vittorio, A flexible carbon nanotubes-based auxetic sponge electrode for strain sensors, Nanomaterials 10 (12) (2020) 2365.
[23] M. Wan, K. Yu, H. Sun, 4D printed programmable auxetic metamaterials with shape memory effects, Compos. Struct. 279 (2022) 114791.
[24] X. Tan, S. Chen, B. Wang, J. Tang, L. Wang, S. Zhu, K. Yao, P. Xu, Real-time tunable negative stiffness mechanical metamaterial, Extreme Mech. Lett. 41 (2020) 100990.
[25] Q. Li, D. Yang, C. Ren, X. Mao, A systematic group of multidirectional buckling-based negative stiffness metamaterials, Int. J. Mech. Sci. 232 (2022) 107611.
[26] S. Lin, Y. Zhang, Y. Liang, Y. Liu, C. Liu, Z. Yang, Bandgap characteristics and wave attenuation of metamaterials based on negative-stiffness dynamic vibration absorbers, J. Sound Vib. 502 (2021) 116088.
[27] T. Jiang, Q. Han, C. Li, Design and compression-induced bandgap evolution of novel polygonal negative stiffness metamaterials, Int. J. Mech. Sci. (2023) 108658.
[28] L. Salari-Sharif, B. Haghpanah, A.G. Izard, M. Tootkaboni, L. Valdevit, Negative-stiffness inclusions as a platform for real-time tunable phononic metamaterials, Phys. Rev. Appl. 11 (2) (2019) 024062.
[29] M. Sun, K. Zhang, X. Guo, Z. Zhang, Y. Chen, G. Zhang, S. Jiang, A novel negative stiffness metamaterials: discrete assembly and enhanced design capabilities, Smart Mater. Struct. 32 (9) (2023) 095036.
[30] D.L. Platus, Negative-stiffness-mechanism vibration isolation systems. Paper read at vibration control in microelectronics, optics, and metrology, SPIE 1619 (1992).
[31] A. Pal, V. Restrepo, D. Goswami, R. Martinez, Exploiting mechanical instabilities in soft robotics: control, sensing, and actuation, Adv. Mater. 33 (19) (2021) 2006939.
[32] S. Chen, X. Tan, J. Hu, S. Zhu, B. Wang, L. Wang, Y. Jin, L. Wu, A novel gradient negative stiffness honeycomb for recoverable energy absorption, Compos. B Eng. 215 (2021) 108745.
[33] D.R. Smith, J.B. Pendry, M.C. Wiltshire, Metamaterials and negative refractive index, Science 305 (5685) (2004) 788–792.
[34] J. Valentine, S. Zhang, T. Zentgraf, E. Ulin-Avila, D.A. Genov, G. Bartal, X. Zhang, Three-dimensional optical metamaterial with a negative refractive index, Nature 455 (7211) (2008) 376–379.
[35] W. Cai, U.K. Chettiar, A.V. Kildishev, V.M. Shalaev, Optical cloaking with metamaterials, Nat. Photon. 1 (4) (2007) 224–227.
[36] J. Christensen, F.J.G. de Abajo, Anisotropic metamaterials for full control of acoustic waves, Phys. Rev. Lett. 108 (12) (2012) 124301.
[37] L. Jin, R. Khajehtourian, J. Mueller, A. Rafsanjani, V. Tournat, K. Bertoldi, Guided transition waves in multistable mechanical metamaterials, PNAS 117 (5) (2020) 2319–2325.
[38] Y. Li, G. Yu, B. Liang, X. Zou, G. Li, S. Cheng, J. Cheng, Three-dimensional ultrathin planar lenses by acoustic metamaterials, Sci. Rep. 4 (1) (2014) 6830.
[39] Y. Zhang, J. Cheng, W. Xu, C. Wang, J. Liu, Y. Li, S. Yang, Particle damping vibration absorber and its application in underwater ship, J. Vib. Eng. Technol. 11 (5) (2023) 2231–2248.
[40] K.K. Bera, A. Banerjee, Active metadamping: a phenomenon of damping enhancement in metamaterial via feedback control, J. Sound Vib. 546 (2023) 117452.
[41] R. Yu, S. Rui, X. Wang, F. Ma, An integrated load-bearing and vibration-isolation supporter with decorated metamaterial absorbers, Int. J. Mech. Sci. 253 (2023) 108406.
[42] S. Chen, X. Liu, J. Hu, B. Wang, M. Li, L. Wang, Y. Zou, L. Wu, Elastic architected mechanical metamaterials with negative stiffness effect for high energy dissipation and low frequency vibration suppression, Compos. B Eng. 267 (2023) 111053.
[43] X. Shen, W.-S. Gan, D. Shi, Multi-channel wireless hybrid active noise control with fixed-adaptive control selection, J. Sound Vib. 541 (2022) 117300.
[44] B. Tang, X. Yu, K. Ye, H. Zhang, Manifold mechanical deformations of organic crystals with optical waveguiding and polarization rotation functions, Adv. Opt. Mater. 10 (2) (2022) 2101335.
[45] W. Liu, Y. Ma, X. Liu, J. Zhou, C. Xu, B. Dong, C. Lee, Larger-than-unity external optical field confinement enabled by metamaterial-assisted comb waveguide for ultrasensitive long-wave infrared gas spectroscopy, Nano Lett. 22 (15) (2022) 6112–6120.
[46] M. Chen, B. Xiao, Y. Feng, T. Yang, H. Zhang, Y. Liu, W. Xu, H. Jiang, Y. Wang, Wave characteristics of reconfigurable elastic metamaterials based on a multi-stable structure, Eng. Struct. 280 (2023) 115715.
[47] W.J. Padilla, R.D. Averitt, Imaging with metamaterials, Nat. Phys. 4 (2) (2022) 85–100.
[48] M. Zhao, B. Ji, D.Z. Zhang, H. Li, H. Zhou, Design and mechanical performances of a novel functionally graded sheet-based lattice structure, Addit. Manuf. 52 (2022) 102676.
[49] H. Liu, E.T. Zhang, G. Wang, B.F. Ng, In-plane crushing behavior and energy absorption of a novel graded honeycomb from hierarchical architecture, Int. J. Mech. Sci. 221 (2022) 107202.
[50] W. Liu, L. Wu, J. Sun, J. Zhou, Origami-inspired quasi-zero stiffness metamaterials for low-frequency multi-direction vibration isolation, Appl. Phys. Lett. 123 (8) (2023).
[51] X. Zhang, J. Ma, M. Li, Z. You, X. Wang, Y. Luo, K. Ma, Y. Chen, Kirigami-based metastructures with programmable multistability, PNAS 119 (11) (2022) e2117649119.
[52] N. Feng, Y. Tie, S. Wang, J. Guo, Z. Hu, Mechanical performance of 3D-printing annular honeycomb with tailorable Poisson's ratio, Mech. Adv. Mater. Struct. 30 (18) (2023) 3781–3789.
[53] N. Feng, S. Wang, Y. Tie, W. Liu, Z. Zhao, J. Guo, Elastic deformability and zero Poisson's ratio within a novel structure inspired by the gardenia from nature, Mech. Adv. Mater. Struct. 1–13 (2022).
[54] H. Zhu, P. Wang, D. Wei, J. Si, Y. Wu, Energy absorption of diamond lattice cylindrical shells under axial compression loading, Thin-Walled Struct. 181 (2022) 110131.
[55] C. Peng, P. Marzocca, P. Tran, Triply periodic minimal surfaces based honeycomb structures with tuneable mechanical responses, Virtual Phys. Prototyping 18 (1) (2023) e2125879.
[56] W. Wang, Y. Jin, Y. Mu, M. Zhang, J. Du, A novel tubular structure with negative Poisson's ratio based on gyroid-type triply periodic minimal surfaces, Virtual Phys. Prototyping 18 (1) (2023) e2203701.
[57] F. Chu, Y. Hou, L. Liu, S. Qiu, W. Cai, Z. Xu, L. Song, W. Hu, Hierarchical structure: an effective strategy to enhance the mechanical performance and fire safety of unsaturated polyester resin, ACS Appl. Mater. Interfaces 11 (32) (2019) 29436–29447.
[58] Z.-P. Wang, L.H. Poh, Y. Zhu, J. Dirrenberger, S. Forest, Systematic design of tetra-petals auxetic structures with stiffness constraint, Mater. Des. 170 (2019) 107669.
[59] R. Gatt, J.N. Grima, K.E. Evans, A. Alderson, On the potential of connected stars as auxetic systems, Mol. Simul. (2005).
[60] P.-S. Farrugia, R. Gatt, D. Attard, F.R. Attenborough, K.E. Evans, J.N. Grima, The auxetic behavior of a general star-4 structure, Phys. Status Solidi B 258 (12) (2021) 2100158.
[61] J. Zhang, D. Karagiozova, Z. You, Y. Chen, G. Lu, Quasi-static large deformation compressive behaviour of origami-based metamaterials, Int. J. Mech. Sci. 153 (2019) 194–207.
[62] X. Ren, R. Das, P. Tran, T.D. Ngo, Y.M. Xie, Auxetic metamaterials and structures: a review, Smart Mater. Struct. 27 (2) (2018) 023001.
[63] Y. Morikawa, S. Yamagiwa, H. Sawahata, R. Numano, K. Koida, M. Ishida, T. Kawano, Ultrastretchable kirigami bioprobes, Adv. Healthcare Mater. 7 (3) (2018) 1701100.

[64] K. Yong, S. De, E.Y. Hsieh, J. Leem, N.R. Aluru, S. Nam, Kirigami-inspired strain-insensitive sensors based on atomically-thin materials, Mater. Today. 34 (2020) 58–65.
[65] A.M. Abdullah, X. Li, P.V. Braun, J.A. Rogers, K.J. Hsia, Kirigami-inspired self-assembly of 3D structures, Adv. Funct. Mater. 30 (14) (2020) 1909888.
[66] Y.C. Cheng, H.C. Lu, X. Lee, H. Zeng, A. Priimagi, Kirigami-based light-induced shape-morphing and locomotion, Adv. Mater. 32 (7) (2020) 1906233.
[67] A. Rafsanjani, Y. Zhang, B. Liu, S.M. Rubinstein, K. Bertoldi, Kirigami skins make a simple soft actuator crawl, Sci. Rob. 3 (15) (2018) eaar7555.
[68] S. Jiang, J. Liu, W. Xiong, Z. Yang, L. Yin, K. Li, Y. Huang, A. Snakeskin-Inspired, Soft-hinge kirigami metamaterial for self-adaptive conformal electronic armor, Adv. Mater. 34 (31) (2022) 2204091.
[69] A.K. Brooks, S. Chakravarty, M. Ali, V.K. Yadavalli, Kirigami-inspired biodesign for applications in healthcare, Adv. Mater. 34 (18) (2022) 2109550.
[70] N. Pagliocca, K.Z. Uddin, I.A. Anni, C. Shen, G. Youssef, B. Koohbor, Flexible planar metamaterials with tunable Poisson's ratios, Mater. Des. 215 (2022) 110446.
[71] F. Lu, B. Lin, X. Ling, C. Zhang, Y. Zhu, Controllable design of bi-material metamaterials with programmable thermal expansion and Poisson's ratio, Compos. Struct. 322 (2023) 117417.
[72] E. Medina, C.H. Rycroft, K. Bertoldi, Nonlinear shape optimization of flexible mechanical metamaterials, Extreme Mech. Lett. 61 (2023) 102015.
[73] A. Montazeri, E. Bahmanpour, M. Safarabadi, A Poisson's ratio sign-switching mechanical metamaterial with tunable stiffness, Int. J. Mech. Sci. 260 (2023) 108670.
[74] Y. Zhao, Y. Chen, Y. Zhou, Novel mechanical models of tensile strength and elastic property of FDM AM PLA materials: experimental and theoretical analyses, Mater. Des. 181 (2019) 108089.
[75] H. Gonabadi, A. Yadav, S. Bull, The effect of processing parameters on the mechanical characteristics of PLA produced by a 3D FFF printer, Int. J. Adv. Manuf. Technol. 111 (2020) 695–709.
[76] J.M. Mercado-Colmenero, M.A. Rubio-Paramio, M.D. la Rubia-Garcia, D. Lozano-Arjona, C. Martin-Doñate, A numerical and experimental study of the compression uniaxial properties of PLA manufactured with FDM technology based on product specifications, Int. J. Adv. Manuf. Technol. 103 (2019) 1893–1909.
[77] X.-L. Peng, S. Bargmann, A novel hybrid-honeycomb structure: enhanced stiffness, tunable auxeticity and negative thermal expansion, Int. J. Mech. Sci. 190 (2021) 106021.
[78] M. Wang, H. Wu, L. Yang, A. Chen, P. Chen, H. Wang, Z. Chen, C. Yan, Structure design of arc-shaped auxetic metamaterials with tunable Poisson's ratio, Mech. Adv. Mater. Struct. 30 (7) (2023) 1426–1436.
[79] N.K. Choudhry, B. Panda, S. Kumar, Enhanced energy absorption performance of 3D printed 2D auxetic lattices, Thin-Walled Struct. 186 (2023) 110650.
[80] N. Feng, J. Yan, Z. Feng, X. Lin, T. Zhang, J.J.M.P. Li, Characterization, Linear in-plane elasticity of a polygon honeycomb core with zero Poisson's ratio, Mater. Perform. Charac. 9 (1) (2020) 711–725.